Sensory design in food 3D printing – Structuring, texture modulation, taste localization, and thermal stabilization

Ahmed Raouf Fahmy [a,1], Laura Sophie Amann [b,1], Andreas Dunkel [c], Oliver Frank [b], Corinna Dawid [b], Thomas Hofmann [b], Thomas Becker [a], Mario Jekle [a,*]

[a] *Technical University of Munich, TUM School of Life Sciences, Chair of Brewing and Beverage Technology, Research Group Cereal Technology and Process Engineering, Weihenstephaner Steig 20, 85354 Freising, Germany*
[b] *Technical University of Munich, TUM School of Life Sciences, Chair of Food Chemistry and Molecular Sensory Science, Lise-Meitner-Strasse 34, 85354 Freising, Germany*
[c] *Leibniz-Institute for Food Systems Biology at the Technical University of Munich, Lise-Meitner-Strasse 34, 85354 Freising, Germany*

ARTICLE INFO

ABSTRACT

Most 3D printing studies of foods deal with the feasibility and modulation of textures independent of flavor design aspects. As a cornerstone for the combined control over texturing and taste distribution, a 3D printing method for starch-based food textures was developed in a pioneering approach using dual extrusion coupled with focused on-board near infrared (NIR) heating for thermal stabilization. The developed method facilitated the design of hydrated starch-egg white powder-systems in reproducible printing configurations. To systematically study the influence of inhomogeneous taste distribution on sensory perception, it was applied in a saltiness sensory contrast study. For the first time, defined concentration gradients of sodium chloride were spatially printed in food textures. Comparable textural properties at the same infill levels were achieved for all printed structures with different sodium localizations. Furthermore, the inhomogeneous spatial distribution of sodium chloride caused saltiness enhancement. This 3D structuring, taste localization coupled with thermal stabilization (3D SLTS) methodology enables the elucidation of texture-taste release interactions.

1. Introduction

Food layered manufacture (FLM) is a food production process where the processing of food is implemented using electro-mechanical based additive manufacturing (AM) approach. To illustrate, additive manufacturing or 3D printing is a process where structures are built layer-by-layer from 3D models. The most commonly used 3D printing technology in the food sector for its ability to structure highly viscous pastes or materials is the fused deposition modeling (FDM) technique which relies on extrusion and deposition principles (ASTM-International, 2012). Moreover, the introduction of rapid prototyping (RP) and additive manufacturing in food production gives the advantage of customization and personalization over traditional processing (Wegrzyn, Golding, & Archer, 2012). Due to the accuracy and precision of the 3D printing technology, complex food structures can be produced incorporating customized textures, tailored nutrition, and functional ingredients (Derossi, Caporizzi, Azzollini, & Severini, 2018; Lille,

Nurmela, Nordlund, Metsä-Kortelainen, & Sozer, 2018; Y. Liu et al., 2019; Zhenbin Liu, Zhang, & Yang, 2018; Sun, Zhou, Yan, Huang, & Lin, L. ya., 2018; Vancauwenberghe et al., 2018, 2019; Zhang, Lou, & Schutyser, 2018). Concerning the development of AM technologies in the production of food systems such as bread, 3D printing can be used to eliminate structural heterogeneity. This structural variability affects reproducibility which impedes the understanding of mechanistic relationships (Zghal, Scanlon, & Sapirstein, 2002). By slicing bulk structures into individual layers, the control over aeration, cellular structure, mechanical properties, and distribution of taste is achievable (Fahmy, Becker, & Jekle, 2020, 2021). Therefore, 3D printing technology has the potential of being applied in the texture and taste design as well as a tool for understanding the texture and taste relationships in food- and cereal-based material systems and structures. However, several technological developments regarding structuring, localization, and on-board thermal stabilization are required to take full advantage of 3D printing in food applications (Baiano, 2020).

---

* Corresponding author.
  E-mail address: mjekle@tum.de (M. Jekle).
[1] A. R. Fahmy and L. S. Amann contributed equally to this work as first authors.

The sensory perception during food consumption depends not only on the concentrations of odor- and taste-active compounds but also on the texture of food matrix (Tournier, Sulmont-rossé, & Guichard, 2007). The possibility of targeted analysis and control of the sensory perception of foods is confined due to limited knowledge about texture-taste interactions. Particularly, the sensory activity can hardly be predicted by the integral overall concentration if taste compounds are heterogeneously distributed in complex food matrices. Thus, it could be shown that inhomogeneous spatial distribution of taste-active compounds causes intensified sensory perception (Konitzer et al., 2013; Noort, Bult, Stieger, & Hamer, 2010; Noort et al., 2012). Noort et al. (Noort et al., 2010) investigated the effects of local concentration gradients of sodium chloride in layered bread on the perceived saltiness intensity. For this purpose, starch-protein layers with varying NaCl contents were stacked in alternating fashion before baking. They reported a significant saltiness enhancement of bread with high NaCl contrasts between layers compared to bread with homogeneous NaCl distribution, allowing up to 28% sodium reduction while maintaining saltiness intensity. The enhancement of salty taste has been ascribed mainly to the sensory contrast and to a small extent to a faster sodium release (Konitzer et al., 2013; Noort et al., 2010; Noort et al., 2012). In these previous studies, a precise positioning of spatial concentration gradients was not possible. The studies were performed with conventional manufacturing techniques on sparsely defined food matrices. To systematically investigate the effect of taste distribution on the sensory perception, new texturing approaches are necessary that achieve highly defined and reproducible texture construction. For this purpose, our study presents an approach which utilizes dual extrusion 3D printing for structuring matrix textures with spatial localization of sensory-active compounds. The method enables the production of highly defined starch-based material systems with targeted incorporation of locally resolved concentration gradients of sodium chloride.

For all food systems, the manipulation of sensory perception through the combined structure and flavor design using 3D printing is yet to be technologically integrated and functionally investigated. Without consideration for the flavor design aspects, most available studies are focused on the feasibility of texture design of foods through 3D printing (Jonkers, Van Dommelen, & Geers, 2020; Le Tohic et al., 2018; Y. Liu et al., 2019; Phuhongsung, Zhang, & Devahastin, 2020; Vancauwenberghe et al., 2018). As an example, Liu et al. (Liu et al., 2019) 3D printed variable textural properties for milk protein composite gels by changing the protein concentration. On the other hand, Vancauwenberghe et al. (Vancauwenberghe et al., 2018) obtained variable textural properties through honeycomb porosity control using varying number of cells and pore sizes. By moving forward from the isolated texture variability research, the combined control over texture and taste distribution, which is developed in this study using dual extrusion, can be a step forward for the coupled manipulation of texture and taste.

For printing of some types of gel systems, thermal stabilization or post-processing is not required for functionality or geometrical stability. On the other hand, for other foods such as starch-based systems, induced heat transitions for thermal stabilization are important for post-printing geometrical stability and consumption (He, Zhang, & Fang, 2020). Considering highly consumed staple products incorporating starch and protein contents, heat stabilization is required for inducing physiochemical changes such as protein denaturation, starch gelatinization and dehydration for storage stability in terms of low water activity and microbial growth. Different 3D food printing studies included thermal stabilization as post-processing in the form of microwave drying, baking, steaming, frying and other methods (He et al., 2020; Lille et al., 2018; Zipeng Liu, Chen, Zheng, Xie, & Chen, 2020; Pulatsu, Su, Lin, & Lin, 2020; Yang, Zhang, Prakash, & Liu, 2018, Yang, Zhang, & Liu, 2019). On the other hand, the on-board integration of thermal stabilization solutions is missing in food printing studies. The term on-board denotes the electromechanical integration of the heating system into the 3D printing system which can lead to the exclusion of post-processing after food

printing. Moreover, the optimized coupling between 3D printing and an on-board thermal stabilization solution can enable layer-based heating, targeted or local heating, and automatic material-based heating optimization. The presented method incorporates a focused on-board near infrared (NIR) stabilization system for geometric stabilization and for achieving process-independent, precisely defined, and reproducible matrix textures.

To utilize the developed 3D printing method with integration of structuring, localization, and thermal stabilization, a saltiness sensory contrast study was carried out. In this approach, local NaCl distributions were spatially printed in hydrated wheat starch-egg white powder-mixtures using alternating layers with different configurations to investigate the influence of inhomogeneous NaCl distribution on sensory perception. Each layer of the printed structures was individually and automatically stabilized using a NIR spot heater before printing the subsequent layer. This automatic heating method was used to thermally and geometrically stabilize the material to reduce diffusion and mechanical deformation. Texture profile analyses were used to investigate possible textural discrepancies between the single and dual extruded structures. The actual sodium content of the samples and different layers was quantified by means of ion chromatography. The starch-based samples with inhomogeneous spatial distribution of sodium were evaluated by human sensory analyses. Finally, the combination of existing knowledge concerning texturing and the successful localization of spatial NaCl concentration gradients can be a milestone for future elucidation of mechanistic texture-taste interactions which was not possible before.

2. Materials and methods

2.1. Raw materials

A material system composed of hydrated wheat starch and egg white powder was used for 3D printing. The wheat starch was provided by Kröner-Stärke GmbH (Ibbenbüren, Germany). The hen egg white powder was purchased from Bulk Powders (Colchester, United Kingdom). For sensory analyses, an egg white powder with a lower salt content was obtained from FunCakes (Wormer, The Netherlands). According to the methods of the American Association of Cereal Chemists international (AACCi), the moisture content (AACCi 44–01) and protein content (AACCi 46–16) were determined. The wheat starch had a moisture content of $13.98 \pm 0.17\%$ ($n = 3$) and a protein content of 0.27% ($n = 1$; dry mass), and a NaCl content of $0.058 \pm 0.001\%$ ($n = 3$; dry mass). The egg white powders had a moisture content ($n = 3$) of $6.88 \pm 0.03\%$ (Bulk Powders) and $8.49 \pm 0.21\%$ (FunCakes), a protein content ($n = 1$; dry mass) of 83.42% (Bulk Powders) and 82.87% (FunCakes), and a NaCl content ($n = 3$; dry mass) of $6.46 \pm 0.06\%$ (Bulk Powders) and $3.34 \pm 0.07\%$ (FunCakes).

2.2. Chemicals

The purity grade of chemicals was pro analysi (p.a.) unless noted otherwise. The following chemicals were commercially obtained: Patent Blue V calcium salt (Glentham Life Sciences Ltd., Corsham, United Kingdom), ethanol (VWR International, Fontenay-sous-Bois, France), methanol (HPLC grade; J. T. Baker, Griesheim, Germany), sodium chloride (Sigma-Aldrich GmbH, Steinheim, Germany), D-sucrose (Carl Roth GmbH & Co. KG, Karlsruhe, Germany), caffeine (Merck KGaA, Darmstadt, Germany), monosodium L-glutamate (Alfa Aesar, Ward Hill, USA), ferulic acid and L-lactic acid (Fluka GmbH, Neu-Ulm, Germany). Water for mixture preparation, extraction, dilution steps, and analysis was purified using a Milli-Q Reference A+ Water Purification System (Merck Millipore, Darmstadt, Germany). Evian® water, a commercially available table water with low mineral content, was used for sensory analysis.

2.3. Desalination of egg white powder by means of ultrafiltration

A portion (7.5 g) of egg white powder (FunCakes, Wormer, The Netherlands) was homogenized in 250 mL ethanol/water (20/80, *v*/v) with an Ultra-Turrax (12,000 rpm, 1 min). The suspension was filled in a Vivacell 250 static gas pressure ultrafiltration concentrator (Sartorius AG, Göttingen, Germany) equipped with a Vivacell 250 polyethersulfone membrane (5 kDa) that was preconditioned by rinsing the membrane with deionized water (3 × 200 mL). After sealing, nitrogen pressure (3.5 bar) was applied by means of an air pressure controller. During filtration, the Vivacell 250 device was agitated (100 rpm, room temperature) on an orbital shaker (type 3005, GFL, Burgwedel, Germany). The retentate was taken up in 20% aqueous ethanol solution (200 mL) and was once more ultrafiltered under pressure (3.5 bar). This washing step was repeated twice. After filtration, the retentate was removed from the ultrafiltration device and the membrane was washed with deionized water to recover absorbed material. Afterwards, the solubilized retentate was lyophilized. The different batches of desalted egg white powder were combined and homogenized (3 h) using a Turbula® shaker mixer (WAB, Muttenz, Switzerland).

2.4. Preparation of printing materials

All starch-protein systems are displayed in Table 1. A total of 11 different starch-based blends was used which consisted of hydrated wheat starch-egg white powder-mixtures (SE) or hydrated wheat starch-desalted egg white powder-mixtures (SDE). The ratio of wheat starch to (desalted) egg white powder was kept at 85:15 (*w*/w) for all printing mixtures (Goesaert et al., 2005; Jekle, Mühlberger, & Becker, 2016). The overall NaCl content of the mixtures is listed in Table 1 and is given in g/100 g on dry material (starch and egg white powder) to provide values that are comparable with other studies which express the NaCl content in g/100 g on flour basis.

A Z-type kneader (63 rpm) was used to prepare the different mixtures. A pre-mixing step (1 min) was used to mix the dry ingredients before adding aqueous NaCl solutions. For the dyed mixtures, Patent Blue V calcium salt (50 mg) was added to the solutions and stirred on a

magnetic stirrer (5 min). After adding the solutions, the mixture was kneaded (10 min), placed in a plastic beaker which was covered using Parafilm (Bemis Company Inc., Wisconsin, USA), and left to rest (30 min, room temperature) until the preparation and assembly of both extruders was completed. Concerning the characterization, printability, and textural analyses experiments, the mixtures were prepared and measured in triplicates. Throughout this paper, the naming scheme or abbreviations mentioned in Table 1 was used to denote the different mixtures.

2.5. 3D printing setup, process, and experiments

For this study, an X400 V3 3D printer (German RepRap GmbH, Feldkirchen, Germany) was used for printing the starch-based material systems. For all printing experiments, a nozzle diameter of 0.84 mm, a printing speed of 10 mm/s, and an extrusion width/height of 0.84 mm were used. The detailed printing setup including pre-printing calibration was mentioned in our previous study regarding a method development for cereal printing quality analysis (Fahmy et al., 2020). For extrusion and deposition of the mixtures, two progressive cavity pumps (PCP) based extruders were used. Both extruders were purchased from ViscoTec GmbH (Töging, Germany) which are identical except for the pumping chamber size (rotor and stator). The Vipro-head3 and Vipro-head5 extruders have theoretical flow rates of 0.3 to 3.3 mL/min and 0.5 to 6.0 mL/min, respectively. Also, the mentioned flow rates depend on the viscoelastic properties of the extruded materials and the primary flow pressure developed inside the extruder. After conducting the optimization experiments (Fahmy et al., 2020), the extrusion multiplier for the primary extruder (Vipro-head3) was set to 29% while 12% for the secondary extruder (Vipro-head5). Concerning the on-board NIR stabilization, a variable output power 150 W spot heater was used (Optron GmbH, Garbsen, Germany). The used NIR-emitter has a peak wavelength of approximately ~0.98 μm. A control unit was used to interface between the heater and the 3D printer. The heating power is controlled through a variable DC input of 0 to 10 V which is then mapped on the printer's firmware to a pulse width modulation (PWM) of 0 to 213 (0 to
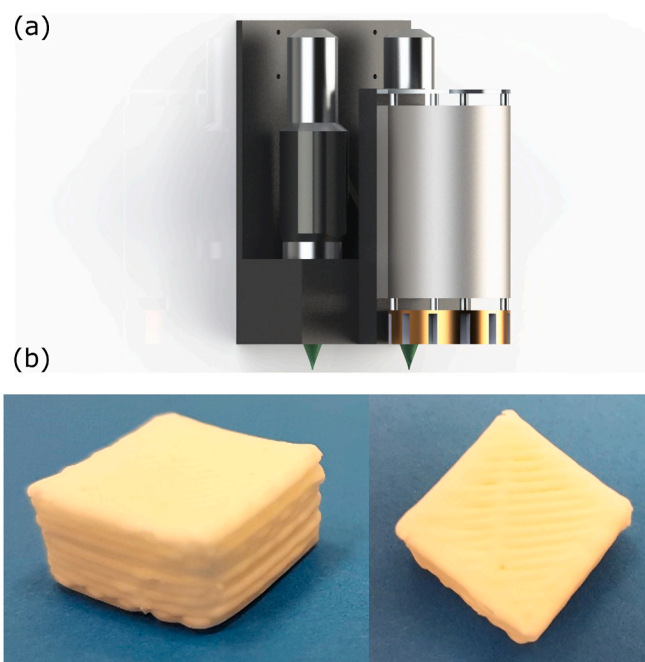
Table 1
Constituents and sodium chloride content of the hydrated wheat starch-egg white powder-mixtures (SE) and the hydrated wheat starch-desalted egg white powder-mixtures (SDE) for 3D printing.

Abbreviations	Description	Wheat starch (g) – (desalted) egg white powder (g) – aqueous solution (g) – food dye (g)	NaCl content (g/100 g dry material)
SE60	SE without NaCl	85–15–60–0	0.66 ± 0.05 [e]
SE60-Med	SE + medium NaCl	85–15–60–0	1.92 ± 0.08 [c]
SE60-Hi	SE + high NaCl	85–15–60–0	3.07 ± 0.12 [a]
SE60-DYE	SE + dye	85–15–60–0.05	0.63 ± 0.05 [e]
SE60-Hi-DYE	SE + high NaCl + dye	85–15–60–0.05	3.13 ± 0.11 [a]
SDE102	SDE without NaCl	85–15–102–0	0.16 ± 0.02 [f]
SDE96-Med	SDE + medium NaCl	85–15–96–0	1.20 ± 0.13 [d]
SDE94-Hi	SDE + high NaCl	85–15–94–0	2.44 ± 0.20 [b]
SDE102-DYE	SDE + dye	85–15–102–0.05	0.19 ± 0.02 [f]
SDE96-Med-DYE	SDE + medium NaCl + dye	85–15–96–0.05	1.11 ± 0.11 [d]
SDE94-Hi-DYE	SDE + high NaCl + dye	85–15–94–0.05	2.46 ± 0.20 [b]

NaCl content is expressed in mean ± standard deviation. Means with unequal letters (a - f) are significantly different ($p < 0.05$).

Fig. 1. Printing head and images of a 3D printed cuboid: (a) 3D rendering of the mounting system including the dual PCP extruders, and NIR spot heater; (b) images of a 3D printed sample at 100% infill with localized sodium using dual extrusion and NIR heating.

12 V corresponds to PWM or 0 to 255).

As shown in Fig. 1, a mounting system was printed using PLA to accommodate both extruders sideways while the spot heater was mounted in the perpendicular direction. With respect to the primary extruder, the secondary extruder was mounted with an offset of 80 mm in the x-direction while the spot heater was mounted with an offset of 40 mm and 30 mm in the x- and y-directions, respectively. The offset of the secondary extruder was accounted for in the printer's firmware. Layer- and tool-change G-code scripts were used, where the offsets were accounted for, to accommodate the layer-based heating routines. These scripts were executed during layer changes, whether there is a tool change or not, to insure a uniform layer-based heating and thermal stabilization.

For the printing of the starch-protein-based structures, a cuboid design of $15.0 \times 15.0 \times 7.5$ mm (L × W × H) was used. The infill of all cuboids was 100% for the sensory and chemical analyses. While for the textural analysis, 75% infill cuboids with a middle square cutout beside the 100% infill were used to simulate the different levels of textural properties. The two infill levels were chosen for determining the textural properties produced by dual extrusion compared to single extrusion and to identify and characterize any possible defects arising from the usage of a dual extrusion system. As shown in Fig. 2, five different layer configurations were used for printing the cuboid design at adaptable printing settings. Two designs with homogeneous distribution of sodium chloride were printed using a single extruder (configuration: full a and b). The other designs incorporated a heterogeneous distribution of sodium using dual extrusion with the SE and SDE mixtures (Table 1) acting as the base material. For the 4/4 design shown in Fig. 2, the first four layers (bottom layers) were printed using the SE60 and SDE102 (Table 1) while the top 4 layers (top layers) were printed using the mixtures containing sodium chloride. The 2/2 and 1/1 designs were printed using a similar approach like the 4/4 design but with alternating dual or single layers, respectively.

2.6. Material characterization and printability experiments

The viscoelastic properties of the different mixtures were characterized using oscillatory measurements on an AR-G2 rheometer (TA instruments, New Castle, USA) coupled with a DIN concentric cylinder. The measurement geometry had a rotor radius of 14 mm and the gap clearance was set to 1 mm. A constant temperature (21 °C) was used through a Peltier plate system. 7 g samples were placed in the measuring cylinder, and the gap was adjusted to 1 mm. A 15 min of resting time was allowed, to replicate the extruder preparation before printing. In addition, a frequency sweep was used at a constant strain of 0.01. The chosen strain level was determined prior to the frequency tests (results not shown) using a strain sweep to characterize the material's linear viscoelastic region. A frequency ranging from 0 to 10 Hz was used. All printed mixtures were measured in triplicate. Furthermore, the onset gelatinization temperature of 58.96 ± 0.44 °C was measured using differential scanning calorimetry (DSC) and the base material (SE60). The DSC measurement was performed according to the method described by Paulik et al. (Paulik et al., 2019).

Since the addition of the sodium solutions and the ultrafiltration process affect the hydration and rheological properties of the starch-based blends and the egg white protein, respectively (Ferreira Machado et al., 2007; Mmadi, Amza, Wang, & Zhang, 2014; Thammasena, Fu, Liu, & Liu, 2020), hydration tests in the form of frequency sweeps were performed. The purpose of the hydration tests was to obtain comparable viscoelastic properties to ensure a similar printing performance between the different mixtures.

A camera-based approach was used to characterize the printing performance of the different starch-based blends used in the present study. This quality characterization approach was presented in a previous study by Fahmy et al. (Fahmy et al., 2020). The quality characterization was performed on lines and stacked lines. The lines were used to characterize the geometric stability of the material formulations. The stacked lines were used to assess the collapse/slumping and the overall
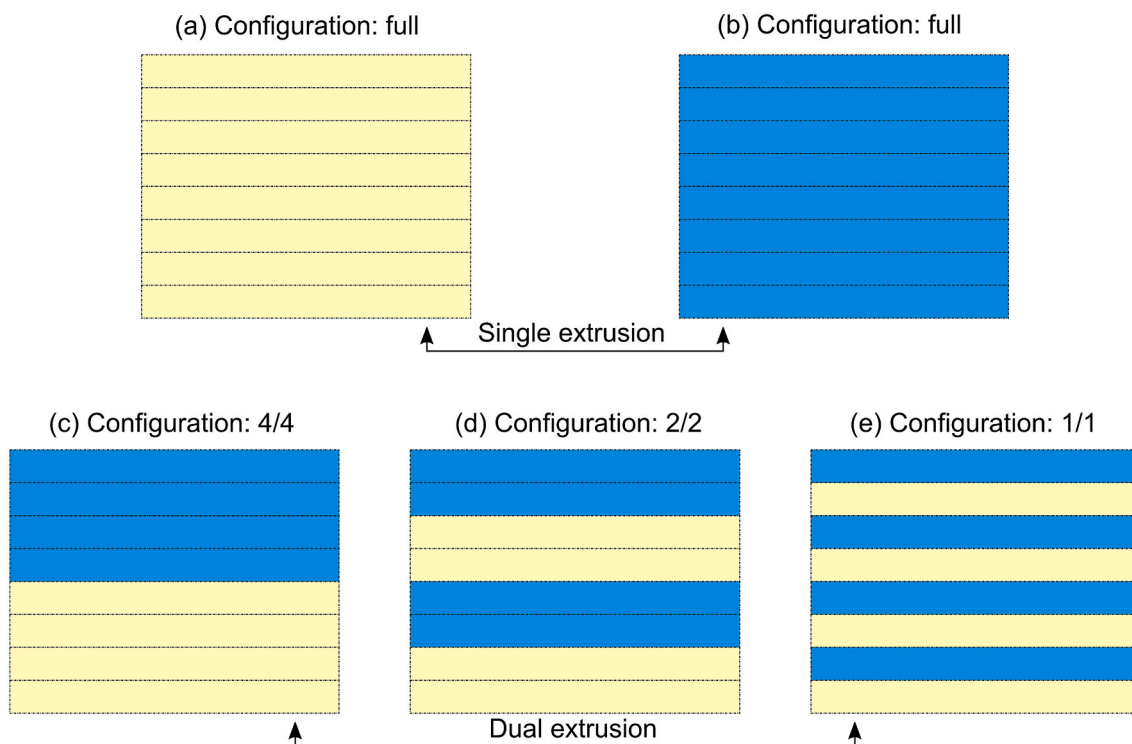

Fig. 2. Schematic diagram of the 3D printed layer configurations: (a) full configuration without dye or sodium addition; (b) full configuration with dye or/and sodium addition; (c) 4/4 configuration with alternating layers of 4; (d) 2/2 configuration with alternating layers of 2; (e) 1/1 configuration with single alternating layers.

structural stability (Fahmy et al., 2020). Geometrical parameters such as the output width, length, and height are extracted and processed autonomously with respect to the input parameters as a point of reference. Other aspects are evaluated such as pre-defined viscoelastic induced defects in the form of over-, under-extrusion, and structural collapse parameters. All measurements were performed with and without NIR heating. All mixtures were printed using a single extruder and measured in triplicate.

2.7. Thermal stabilization

An on-board NIR spot heater was used for thermally stabilizing the printed starch-based structures. The NIR spot heater is composed of a single lamp and a reflector heating system. It has a focal length of 17 mm and a spot diameter of 6 mm, as shown in Fig. 3. The heater was directly connected with the 3D printer's board, as mentioned in Section 2.5, which does not allow for controlling the heater's state, power, or movement in parallel to the printing process. Therefore, a layer-based stabilization approach was used. After each layer is printed, the heating process takes place then the printing is resumed.

For all printed layers, the heater distance was set at the focal length of the reflector (17 mm). A square function was implemented to cover the square's surface area. The square function has a period equivalent to the spot diameter and a phase shift of $-45°$ to insure uniform heating across the surface area.

To select the heating parameters, the heating profiles were measured at different power settings (data not shown). Also, the temperature inside the bottom layer of the printed structures was quantified to evaluate the heat cycles and temperature profiles during printing. For all temperature measurements, a K-type thermocouple was used with a data acquisition device 16-Bit USB DAQ (NI USB-6210) using a LabVIEW software (National Instruments, Texas, USA). The thermocouple was placed approximately at a height of $\sim$0.5 mm of the first layer (middle of bottom layer). A heating power of 32% and movement speed of 13 mm/s (heating time of 4.4 s) for the 100% infill was chosen based on a resultant moisture content level of 41.02 ± 0.28%. Moreover, the speed was calibrated for the material systems with increased hydration to reach the same output moisture level. To obtain a constant moisture content for both printed infill levels (100% and 75%), the heating speed was varied from 9 to 15 mm/s with a step size of 1 mm/s. The different heating speeds were applied to cuboids of 90% infill with grid internal structures. The moisture content of the printed cuboids was measured, according to the AACCi 44–01 standard, at different heater movement speeds to characterize the relation between the heating speed and the occurring moisture loss. Then, to investigate the dependency of moisture loss on the infill variation, the moisture content was measured as the infill was varied between 100 and 80% with a step size of 5% while the heating speed was kept constant at 13 mm/s. Based on the relation between the heating speed, infill, and moisture content, linear regressions were used to obtain a speed calibration equation: $s = ((172.54 - i)/$
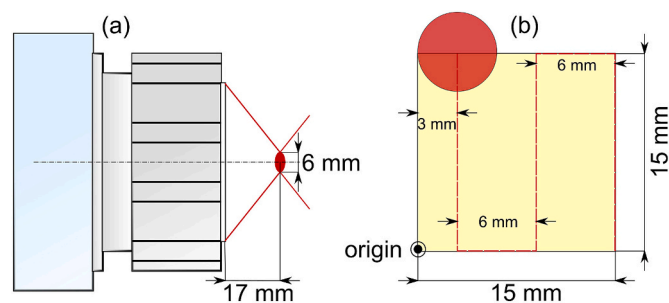
6.385) (1). Where s is the movement speed [mm/s] and i is the infill level (%). Using the mentioned equation, the 75% infill cuboids were printed using a heating speed of 15.34 mm/s (heating time of 3.8 s) to obtain a similar moisture content (compared to the 100% infill) of 40.89 ± 0.79%. In this study, the heating speed calibration was done without consideration for the heat induced transitions of the starch and egg white protein. Finally, all temperature measurements were done in triplicate.

2.8. Texture profile analysis

The textural properties of the printed starch-based systems were characterized using a Texture Analyzer type TA.TX. plus (Stable Micro Systems Ltd., Godalming, UK) with a 50 kg measuring cell. The compression test was performed using an uncoated 25 mm PMMA stamp. A single double compression test was used at a test speed of 2 mm/s and a trigger force of 0.05 N. All the samples were compressed to 10% of its original height at room temperature of 18 ± 2 °C. The test was performed on a full configuration (Fig. 2) of 75% (middle square cutout) and 100% infill using the SE and SDE mixtures, shown in Fig. 2 and Table 1, respectively. The measured forces were recorded with respect to the change in time and distance. To obtain the engineering Young's modulus E, the force-distance curves were converted into stress-strain using the following equation: $\sigma/\varepsilon = ((F/A)/(\Delta H/H))$ (2) (Attenburrow, Goodband, Taylor, & Lillford, 1989; Beer Jr., DeWolf, & Mazurek, 2011). Where σ is the stress [Pa], ε is the strain, F is the resultant force [N], A is the surface area [m^2], H is the sample height [m], and ΔH is lateral deformation [m]. A linear regression was used to obtain the engineering Young's modulus E from the linear section of the stress-strain curve with a coefficient of regression higher than 0.95. From the force-displacement curve of the double compression-decompression cycle, the following textural attributes were determined: hardness (HA), cohesiveness (CO), and resilience (RE). The hardness was extracted from the peak force of the first cycle. Moreover, the cohesiveness was defined as the area ratio of the second compression to the first compression. Finally, the resilience was represented as the ratio of energies equivalent to the ratio of decompression and compression cycles (Kramer & Szczesniak, 1973; Peleg, 2019). All texture measurements were done in triplicates.

2.9. Extraction of mixtures and printed samples

All raw materials, the starch-based blends in all compositions (cf. Table 1), and 3D printed samples in all layer configurations (Fig. 2) were extracted in order to quantify the sodium content. Prior to extraction, the stained inhomogeneous samples were separated in stained and unstained layers based on visual identification and analyzed individually. A portion (0.5 g) of the separated layers was extracted as detailed in the following but with an aliquot of 3.5 mL methanol/water (70/30, v/v). A portion (1.0 g) of each sample was placed in a bead beater tube (CK28_15 mL, Bertin Instruments, Montigny-le-Bretonneux, France) filled with ceramic balls (2.8 mm i. d.). An aliquot (7 mL) of methanol/water (70/30, v/v) was added. The samples were homogenized (6400 rpm, 3 cycles, 30 s each with 30 s breaks, 10 °C) using a bead beater (Precellys Evolution, Bertin Instruments, Montigny-le-Bretonneux, France) and extracted at an orbital shaker (500 rpm, 60 min, room temperature). After centrifugation (4000 rpm, 10 min), the supernatant was removed. The residue was extracted two more times (methanol/water, 70/30, v/v, 7 mL) in the same way as detailed above. The combined supernatants were evaporated to dryness under nitrogen. The remaining extract was dissolved in water and membrane-filtered (0.45 μm). Appropriate dilutions were prepared with water before analysis using High Performance Ion Chromatography (HPIC). The extraction was performed in biological triplicates.

Fig. 3. Schematic diagram of the heating source and process: (a) side view of NIR spot heater and installed reflector with spot diameter of 6 mm; (b) top view of heating routine using a square wave function.

2.10. Quantitative analysis of sodium by means of High-Performance Ion Chromatography

Sodium was quantified by means of HPIC using an ICS-2000 ion chromatography system (Dionex GmbH, Idstein, Germany) with an AS-AP autosampler, an eluent generator equipped with an eluent generator cartridge methanesulfonic acid EGC III MSA, a cation self-regenerating suppressor CSRS 500 (2 mm, suppressor current: 6 mA), and a digital conductivity detector DS6. System control and data processing were carried out using Chromeleon software (version 7.2, Dionex GmbH, Idstein, Germany). The quantification was performed using an external calibration with sodium standard solutions ranging from 1.4 to 175 mg/L. Aliquots (2 µL) were injected into the ICS-2000 apparatus equipped with a Dionex IonPac CS19 analytical column (4 µm, 2 × 250 mm) and a Dionex IonPac CG19 guard column (2 × 50 mm). Chromatography was performed at 30 °C with isocratic elution of aqueous methanesulfonic acid (7 mmol/L) at a flow rate of 0.25 mL/min. The quantitative data is given as the mean of triplicates.

2.11. Analytical sensory experiments

2.11.1. General conditions

All sensory sessions were performed in an air-conditioned sensory room separated into single booths at 20–22 °C. The light was adjusted to yellow to mask visual differences between the samples. The panelists used nose clips to avoid cross-modal interactions with odor-active compounds. The sensory panel consisted of 16 experienced human assessors (aged 24–31 years) who had given informed consent to participate in the sensory tests of the present investigation and have no history of known aroma and taste disorders.

2.11.2. Panel training

The panelists were trained to recognize and evaluate the taste of supra-threshold solutions of following taste compounds in bottled water to become familiar with the taste language used: NaCl (20 mmol/L) for salty taste, D-sucrose (20 mmol/L) for sweet taste, L-lactic acid (20 mmol/L) for sour taste, caffeine (2 mmol/L) for bitter taste, monosodium L-glutamate (6 mmol/L) for umami taste, and tannic acid (0.05%) for puckering-astringent. Furthermore, the panelists were accustomed to the starch-based food matrix and trained to distinguish between a sample with 1.0 g/100 g NaCl on dry material (= %) and samples with different NaCl contents (1.1%, 1.2%, 1.3%, 1.5%, 1.7% and 2.0%) by means of two-alternative forced choice (2-AFC) tests. For this one-sided paired comparison test, mixtures were prepared with wheat starch, low salt egg white powder (FunCakes), and aqueous NaCl solutions in a composition of 53.125/9.375/37.5 (w/w/w). The NaCl content in the samples is given based on the weight of dry materials (= 100%). The starch-based blends were baked in baking tins (50 × 20 × 20 mm, L × W × H) at 230 °C for 10 min. The samples were left to cool for 2 h and stored in airtight freezer bags at 4 °C until the next day. The crust was removed, and the crumb was separated into cubes (7.5 × 7.5 × 7.5 mm, L × W × H) before sensory analysis. To train the panelists, the 2-AFC tests were performed three times.

2.11.3. Saltiness evaluations of 3D printed samples

Before sensory analysis, the 3D printed samples were stored vacuum-packed at −22 °C for maximum 3 days. The perceived saltiness of 3D printed samples with homogeneous and heterogeneous spatial sodium distribution which had the same overall sodium content was compared in 2-AFC tests. For this two-sided paired comparison test, each panelist got a homogeneous sample with medium sodium content (SE60-Med or SDE96-Med) and an inhomogeneous sample consisting of layers without sodium addition (SE60 or SDE102) and layers with high sodium content (SE60-Hi or SDE94-Hi). The inhomogeneous samples in the three different layer configurations, 1/1, 2/2, and 4/4 (Fig. 2), were compared to the homogeneous sample in individual 2-AFC tests.

2.11.4. Procedure of two-alternative forced choice tests

The saltiness evaluation of the samples was carried out by means of 2-AFC tests. In this paired comparison test, the panelists received two covered beakers encrypted by a three-digit random number containing different samples (7.5 × 7.5 × 7.5 mm, L × W × H). To eliminate interfering carry-over effects, the panelists rinsed their mouths with bottled water between tasting of the samples. The panelists were instructed to indicate which of the two samples tasted saltier according to the forced choice method. The statistical evaluation of the 2-AFC tests was performed according to significance tables for one-sided and two-sided paired comparison tests in accordance with ISO 5495 (*ISO 5495: Sensory Analysis – Methodology – Paired Comparison Test. Geneva, Switzerland: International Organization for Standardization*, ISO 5495, 2005). The tables outline the minimum number of correct answers that is required to achieve a significant difference with a specified number of panelists on a level of significance α. Depending on the number of correct answers, the significance level α was determined. All p values ≤ 0.05 were judged as significant.

2.12. Statistics

One-way ANOVA and Tukey's pair-wise comparison, with the significance level set at $p < 0.05$, were used to analyze differences between sodium and NaCl contents. All data and statistical analyses were performed using MATLAB (The MathWorks Corporation, Natick, USA) and OriginPro 2020 (OriginLab Corporation, Northampton, USA).

3. Results and discussion

3.1. Rheological properties and printing performance

Printability tests of 2 different cereal-based systems coupled with rheological characterization were performed at different hydration levels in previous studies (Fahmy et al., 2020; Fahmy, Becker, & Jekle, 2018; Fahmy, Becker, & Jekle, 2019). The base material/mixture used in the presented study (SE60), with a hydration level of 60 g/100 g of dry material, was selected based on its geometric stability and low induced defects during printing. To obtain comparable geometric stability for the printed cuboids of the desalted egg white powder and the different sodium concentrations, the viscoelastic properties were measured through frequency sweeps at different hydration levels (Section 2.4). The hydration levels were varied from 90 to 110 g/100 g of dry material with a step size of 2 g/100 g of dry material according to preliminary tests (not shown). The hydration levels were increased until comparable viscoelastic properties (compared to the base material) were reached. The addition of the 50 mg of Patent Blue V calcium salt was not considered for the rheological hydration tests as there was no significant difference in the observed viscoelastic properties compared to the addition of the sodium base solution.

The viscous component or loss modulus was considered as the point of reference for obtaining the hydration levels for the other mixtures containing the sodium solutions as well as the desalted egg white powder. For reflecting the viscous properties of the materials, the loss modulus was considered over the storage modulus to obtain comparable viscous response of all materials during extrusion and deposition. Furthermore, the flow index could not be considered as the reference for obtaining the hydration levels due to the variation of the shear thinning behavior caused by the functional changes that were introduced by the desalination process, freeze drying, and the different sodium concentrations. For the stock (without sodium) desalted egg white powder mixture SDE102, a hydration level of 102 g/100 g of dry material was observed which corresponds to the same viscosity level of the base SE60 material as shown in Fig. 4. For the medium and high sodium concentration mixtures, the hydration levels were determined as 96 g/100 g SDE96-Med and 94 g/100 g SDE94-Hi of dry material, respectively, for the same viscous levels as the SE60 mixture. An increase in the hydration
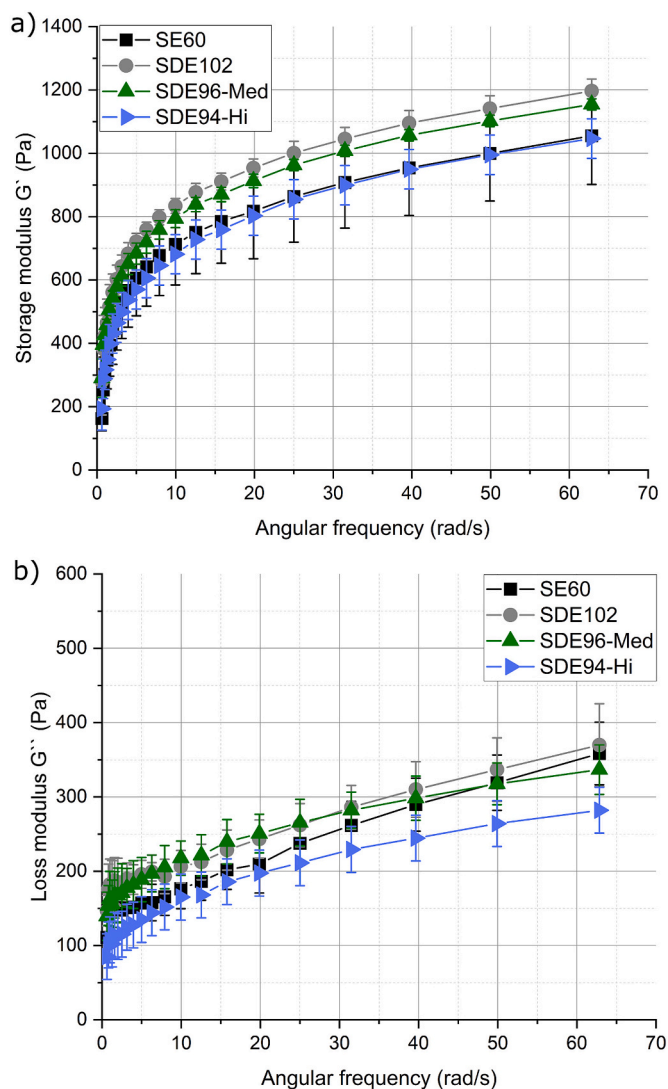
Fig. 4. Frequency sweep of the starch-based blends SE60, SDE102, SDE96-Med, and SDE94-Hi mixtures within 0 and 62 Hz at 21 °C: (a) elastic component; (b) viscous component.

for the SDE mixtures can be contributed to the alteration of the protein's particle microstructure and the protein's hydration properties after the ultrafiltration-desalination (Thammasena et al., 2020). Also, the protein solubility in the purified water compared to the different saline concentration affects the protein-protein and protein-solvent interactions which influences the physiochemical properties and thus the functional properties such as the viscoelastic response of the material (Ferreira Machado et al., 2007; Kakalis & Regenstein, 1986). Depending on the type and content of the present salts in the medium, they affect the electrostatic interactions among the macromolecules through ionic forces and are sufficient to change the conformation of the proteins (Fennema, 1993; Kinsella, 1982). Consequently, the material functionality of the starch-based mixtures is highly influenced by the presence of sodium in different concentrations (Jekle, Necula, Jekle, & Becker, 2019).

After determining the hydration levels for the desalted egg white powder mixtures, the printing quality of the mixtures was analyzed. The dimensional parameters and defects were determined using the on-board camera-based morphological approach as shown in Section 2.6. The approach was used during printing of the lines/stacks before and after the NIR heating. The aim is to highlight the improvement in structural stability of the printed structures after heating, also to detect

any heating induced defects which could influence the structural and textural properties of the printed cuboids.

All output geometrical properties were analyzed and compared to the neutral profile which represents the optimal values of the given parameters. Considering the printed lines and stacks without heating, all materials show signs of slumping or structural collapse with the increasing number of layers, as shown in Fig. 5(a) and (b). The output extruded height (Fig. 5a) for all mixtures decreases from the target value starting from the 3rd layer onwards with the maximum deviation at the 5th layer for the SDE94-Hi mixture with an output height of 3.24 ± 0.03 mm. Compared to the neutral profile at the 5th layer with 4.2 mm in height, the deviation maxes out at approximately 22.8%. This effect indicates the structural collapse under the increasing applied hydrostatic pressure due to the increase in height. Moreover, shown in Fig. 5 (b), all mixtures show a high increase in the width of the printed structures while the optimal width should remain 0.84 mm according to the nozzle diameter under ideal material conditions. For all mixtures, an increase in the extruded width is observed at the deposition of a single layer. This effect can be contributed to the constriction of the nozzle's tip which induces a binding force acting on the material before deposition. The viscoelastic flow of the material causes a die swell phenomenon to occur where the deposited diameter is larger than the channel size (Wang, 2012). This increase can affect the precision of sodium localization if an area-based localization is performed where the local concentration of sodium is located beside or within the base material. On the other hand, for the layer-based approach presented in this study, the die swell effect should not affect the planar localization of the sodium component. Moreover, the maximum deviation of the output width of 1.8 ± 0.3 mm which represents an approximately ~114% increase than the neutral profile for the SE60 mixture at 4 layers. This shows a material flow from the top to the bottom layers in the direction of the gravitational forces. The flow of material between layers under hydrostatic pressure would pose a problem in the localization of the sodium containing mixtures which could nullify the localization of the sodium component. Consequently, the increase in width and decrease in height of all mixtures highlights the importance of a layer-based material stabilization.

The trials involving layer based NIR heating show a large improvement in the height and width performance, as illustrated in Fig. 5(a) and (b). Each layer is autonomously stabilized using the spot heater before the deposition of the consecutive layer. The heat and mass transfer during the localized heating process in the form of temperature increase and moisture loss increases the overall complex modulus of the material towards gelation (results not shown). This increases the yield point for the materials while exposed to the hydrostatic pressure from the height increase during layering of the materials which results on a more stable structure resistant to slumping or structural collapse. Regarding the width of the extruder mixtures with the respect to the increase in deposited layers, results show a fluctuation of maximum ~12% situated around the optimal value of 0.84 mm. Finally, the height of all mixtures increased towards the neutral profile compared to the non-heating trials. The maximum deviation of the SDE94-Hi mixture improved by approximately ~14% (absolute value) with a deviation of ~8.8% represented by a height of 3.8 ± 0.2 mm at 5 layers compared to the 4.2 mm of the optimal or theoretical value.

While short IR wave lengths influence the penetration depths, long-wave radiation is essential regarding the mount of transferred energy to the material (Skjöldebrand, Ellbjär, Andersson, & Eriksson, 1988). To illustrate, when the cereal matrix is exposed to infrared waves, the radiation is absorbed, reflected, or scattered. The absorption intensities of the radiative energy are highly dependent on the matrix constituents as well as the radiation's wave length (Riadh, Ahmad, Marhaban, & Soh, 2015). Consequently, the amount of absorbed radiation as well as the received energy is specific to the cereal matrix and heating setup that was used in this study.

To enumerate the effect of the local NIR layer-based heating method,
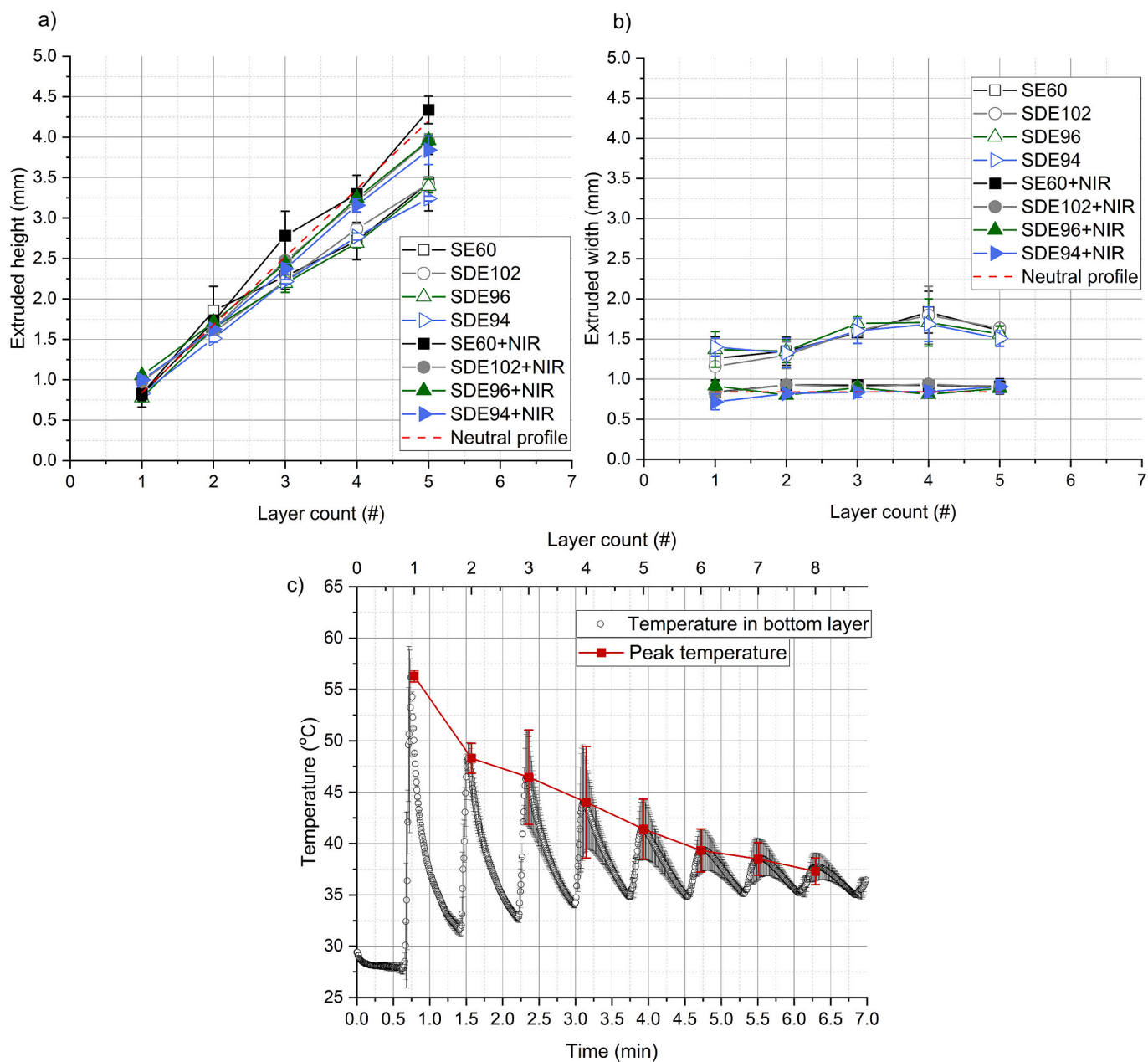
Fig. 5. Printing performance of the printing mixtures and in-line temperature measurements: (a) extruded height of printed stacks up to five layers; (b) extruded width of stacks up to five layers; (c) temperature cycle during printing with respect to the elapsed time and peak temperature recorded during each layer deposition (std $n = 3$).

the heat transmission was measured inside a single layer and through multiple layers. The surface area of the cuboids was decreased to 10.0×10.0 mm but the same layer thickness and structure height was maintained to reduce the printing time while keeping the same heat profiles as the other printing experiments. As shown in Fig. 5(c), the thermal stabilization of each layer consists of heating and cooling cycle. The heating region occurs where the NIR spot is incident to the thermocouple's location. The peak temperature is reached depending on the power and movement speed of the heater corresponding to the amount of time the spot diameter takes to move a length of 6 mm. The cooling cycle represents the heating of other regions followed by the printing of the consecutive layers. Because of this cyclic behavior, the lower layers receive more energy compared to the upper layers. Therefore, a heterogeneous distribution of moisture is expected to occur across the different layers resulting in a concentration gradient of water content

along the thickness direction. Regarding the heat induced transformations, a peak temperature of approximately ~120 °C was measured at the top of the layer (at the focal length of the heater). Using the DSC approach (Section 2.6), the peak gelatinization temperature was observed to be 91.3 °C (extrapolating to the NIR's heating rate). Therefore, this resultant secondary heating cycles that increases proportional to the structure's height means that the heat induced transformation of the starch and protein is different across the layers. Consequently, the mechanical properties are expected to vary across the layers and the structural/textural properties are the resultant of the response of all layers. Furthermore, the concentration gradient of moisture is time dependent where moisture equilibrium occurs with the increase in storage duration. To elucidate the time dependency of moisture equilibrium, the bottom layers of 9 samples were separated directly after printing. Then, 3 samples were measured directly while the

other samples were stored for 1 and 2 days at -22 °C. The sample layers that were measured directly after printing showed a decrease of ~4.5% of the total moisture content compared to the overall moisture content of the cuboids (Section 2.6). After 24 h of storage, the moisture content equilibrated to just a decrease of ~0.3% from the final moisture content. Consequently, the results showed that the sensory tests were conducted where the internal deviations of the moisture content between layers is negligible and thus, moisture content-dependent textural discrepancies are avoided.

3.2. Textural properties

The textural properties of the printed designs and the localized layer configurations were of general interests. Therefore, double compression tests were conducted under quasi-static conditions in the linear deformation regime to texturally characterize the printed cuboids (Section 2.8). Also, the compression tests were used to calibrate the printing process with regards to the operation of the dual PCP extrusion design. The testing and calibration process were of outmost importance to this study as similar or comparable textural properties are required to ensure that the textural differences between the different layer configurations do not influence the results of the sensory analysis so that the results are solely dependent on the localization of the sodium inside the structures.

According to preliminary testing (results not shown), two main factors had an influence on the textural properties and thus they were of great interest to define. First, are the designed offsets in the cartesian coordinates between both custom extruders. Offsets and deviations in the layer height due to the small deviations in the z-axis did not show any influence on the textural properties in the elastic regime. To illustrate, the texture of cereal foams in the elastic regime is mainly dominated by the effective area as well as the relative density (Gibson, 1989; Lorna J. Gibson & Ashby, 1999). The overall height difference due to the propagation of uncertainty in the layer thickness does not affect the texture if the relative density remains constant. Finally, the offsets in the x- and y-axes resulted in high deviations in the output cuboid geometry and textural properties. In relation to the textures, the planar offsets were adjusted until low deviations were achieved. The second influence on the textural properties is derived from the slicing parameters and printing settings. This stems from the material difference contained in both extruders as well as the different flow ratings of both extruders (refer to Section 2.5). The shear rate applied on each material system is different due to the difference in rotor sizes between the extruders and the variability in the flow index or the rate of change of viscosity with respect to the applied shear rate. The flow index variability is a resultant of the functional changes that have arisen from the desalination process, freeze drying, and the different sodium concentrations. The mentioned dependencies affect the deformation of the material micro-structure during extrusion which in turn leads to different output base material properties between both extruders for all localized layer configurations.

To address the dual extrusion induced textural variability, first a constant moisture content (for all layer configurations) was attained through the heating speed optimization method mentioned in Section 2.7. Second, the full configuration (using SE60 and SDE102) was printed using a single extruder (Vipro-head3) controlled with a single set of extrusion and printing settings such as speed, flowrate, etc. On the other hand, full configurations of the sodium containing mixtures were printed using the extruder (Vipro-head5) since in printing the localized layer configuration of 1/1, 2/2, and 4/4 this extruder is used for depositing the sodium containing layers. For this extruder, the slicing/printing settings were adjusted with respect to the output hardness of the printed cuboids for both infills of 75% and 100%. The hardness of the cuboids was compared for all printed full configurations from both extruders and the extrusion settings for the Vipro-head5 extruder were adjusted until there was no significant difference observed. After setting and calibrating the extrusion settings for all mixtures, the cuboids in 75% and 100% infills were printed with the configurations shown in Fig. 2 for the

egg white powder mixture SE60 and for the desalted egg white powder mixture SDE102. Fig. 6 shows the measured textural properties for the SE60 mixture for both infills and all configurations. As shown, comparable textural properties were achieved between the different printed configurations. Consequently, textural deviations between all configurations were eliminated to ensure no influence occurs in the sensory analyses.

3.3. Sodium diffusion in layered samples

Applying the developed 3D printing method, samples with inhomogeneous NaCl distribution were printed in three configurations, 1/1, 2/2, and 4/4 (Fig. 2), consisting of undyed layers without NaCl addition and dyed layers with NaCl addition. The actual sodium content within the different sample layers was quantified to determine whether sodium ions diffuse during the 3D printing and heating process and subsequent storage (cf. Fig. 7). The sodium content of the samples before and after the printing and heating process differ because the sodium content is given based on the fresh weight of the samples and moisture evaporates during the heating process.

In the first approach, a hydrated wheat starch-egg white powder-mixture (SE60) was the base material. The mixture SE60 was used for layers without NaCl addition and SE60-Hi-DYE for layers with NaCl addition (Table 1). The initial sodium concentration ratio between the layers was ~1:5 for all configurations (Fig. 7a). After 3D printing, heating, and storage, the remaining sodium concentration ratio was ~1:2.5 in case of configuration 4/4 and a sodium concentration equilibrium was reached in case of configuration 1/1 and 2/2 (Fig. 7b). This is caused by sodium diffusion from the high to the low salt layers.

In the second and third approach, the base material consisted of a hydrated wheat starch-desalted egg white powder-mixture (SDE102) resulting in a lower sodium content in the layers without NaCl addition compared to the first approach. The difference of approach two and three is the amount of NaCl addition. In both approaches, layers without NaCl addition were printed with mixture SDE102 and layers with NaCl addition were printed with SDE96-Med-DYE in approach two and with SDE94-Hi-DYE in approach three (Table 1). In the second approach, the initial sodium concentration contrast was ~1:7 (Fig. 7c). As a result of sodium diffusion during the 3D printing and heating process and storage, the ratio was reduced to ~1:5 in case of configuration 4/4 and to ~1:1.3 in case of configuration 1/1 and 2/2 (Fig. 7d). In the third approach, the initial sodium concentration ratio between the layers was ~1:15 (Fig. 7e). Due to sodium diffusion, it decreased to ~1:6.4 in case of configuration 4/4, to ~1:4.1 in case of configuration 2/2, and to ~1:3.2 in case of configuration 1/1 (Fig. 7f). Consequently, a large NaCl concentration gradient had to be applied to obtain samples with sodium concentration contrast at the time of sensory evaluation.

Salt diffusion was also reported in literature for layered bread with inhomogeneous NaCl distribution with findings that are comparable with the present study. During fermentation, baking, cooling and storage at ambient temperature, the initial salt concentration ratios of 1:5 and 1:11 of a bread with 1.5 g/100 g NaCl on flour basis were reduced to ~1:2.2 and ~ 1:3.1, respectively (Noort et al., 2010).

The approaches one and three were applied in sensory experiments (Section 3.5) but with uncolored samples. The food colorant was merely added to the high salt starch-based blends of the analysis samples to support the visual layer identification. Patent Blue V calcium salt was used as a food colorant to not alter the sodium content of the printing blends. This was also proven by sodium quantification in mixtures that only differed in addition of dye because no significant difference ($p > 0.05$) occurred between SE60 and SE60-DYE, SE60-Hi and SE60-Hi-DYE, SDE102 and SDE102-DYE, as well as between SDE94-Hi and SDE94-Hi-DYE (Table 1).
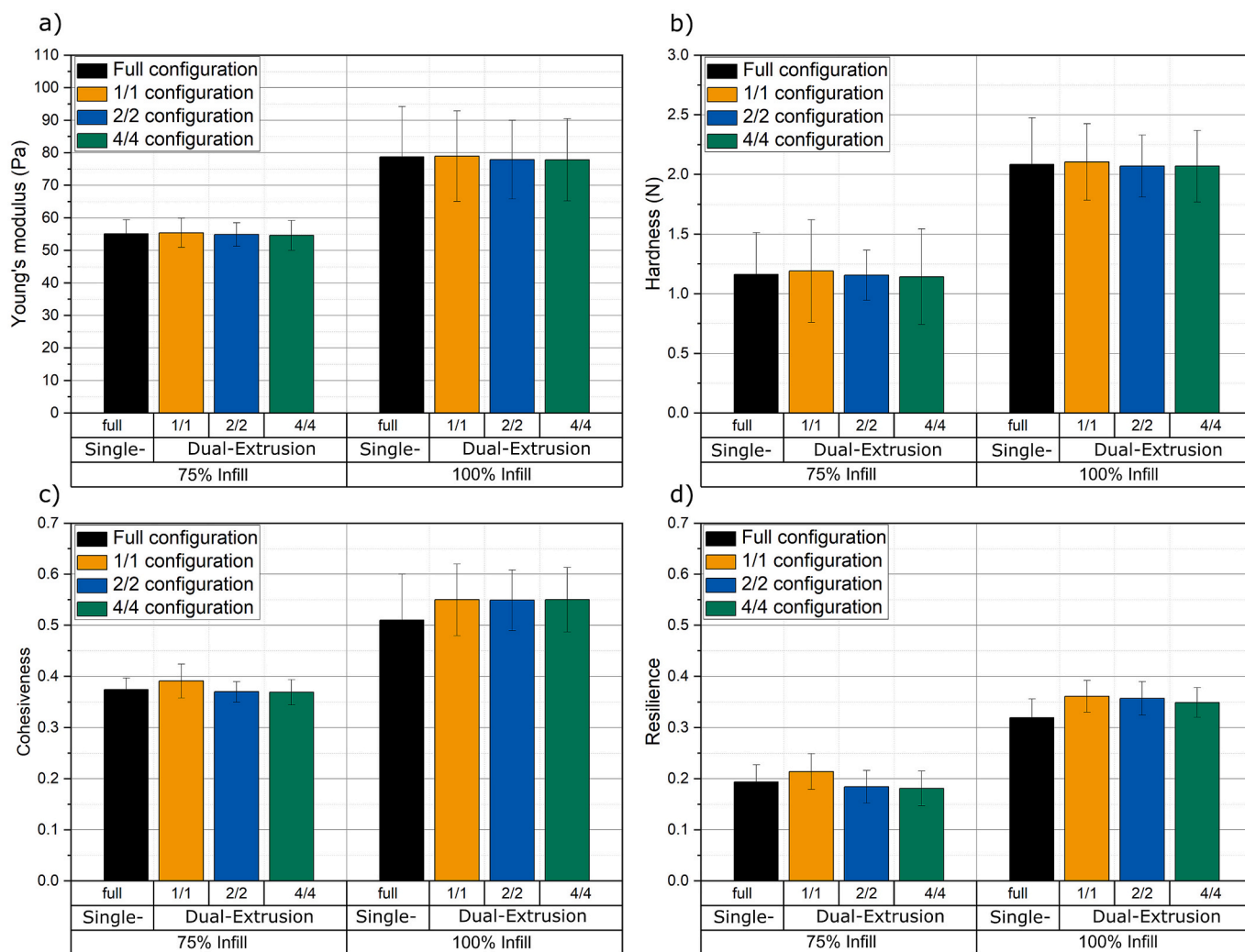
a)

b)

c)

d)

Fig. 6. Texture profile analysis of the 3D SLTS printed configurations from SE mixtures with 75% and 100% infills for all printed configurations: (a) young's modulus; (b) hardness; (c) cohesiveness and (d) resilience.

3.4. Differentiation of samples with variable NaCl contents

To determine the lowest perceivable salt taste difference, the saltiness of a sample with 1.0 g/100 g NaCl on dry material (= %) was assessed in 2-AFC tests in comparison to samples with 1.1%, 1.2%, 1.3%, 1.5%, 1.7%, and 2.0% NaCl, respectively. The samples containing 1.2% NaCl and more were rated significantly saltier ($p = 0.005$ for 1.2% and $p \leq 0.001$ for 1.3%, 1.5%, 1.7%, and 2.0%) than the 1.0% NaCl reference sample. The sample containing 1.1% NaCl could not be significantly distinguished ($p = 0.12$) from the reference sample, thus making 0.2% NaCl the lowest detectable difference for the sensory panel.

3.5. Effect of inhomogeneous spatial distribution of sodium on saltiness perception

By means of 2-AFC tests, the perceived saltiness of 3D printed samples with inhomogeneous spatial sodium distribution in three different layer configurations 1/1, 2/2, and 4/4, was compared to a reference sample with homogeneous distribution containing the same overall sodium chloride content.

In the first sensory experiment, the mixture SE60-Med was used for the homogeneous reference sample and mixtures SE60 and SE60-Hi for the inhomogeneous samples (Table 1). The overall NaCl content of the homogeneous reference sample (1.92 ± 0.08 g/100 g dry material) was

not significantly different ($p > 0.05$) from that of the inhomogeneous samples (1.87 ± 0.05 g/100 g dry material). The sensory panel could not distinguish the homogeneous sample from the inhomogeneous samples of all layer configurations in terms of saltiness ($p \geq 0.5$). The reason for this could be that, at the moment of sensory evaluation, the NaCl concentration gradient between the different layers was too low (ratio ~ 1:2.5) to result in a perceivable effect on saltiness in case of configuration 4/4 and not existent in case of configuration 2/2 and 1/1 because sodium diffusion occurred (Section 3.3). Noort et al. (Noort et al., 2010) reported similar findings in a study with inhomogeneous distribution of NaCl in layered bread. NaCl concentration contrasts of ~1:2.2 and ~ 1:3.1 in breads did not result in a significant difference in the perceived saltiness intensity compared to a homogeneous bread with the same overall NaCl content of 1.5% based on flour.

Previous studies revealed that the saltiness enhancement also depends on the overall NaCl content. The relative saltiness enhancement was strongest at the lowest overall NaCl content (Noort et al., 2010). Because of this, the overall NaCl content was decreased in the second sensory evaluation of the present study by using desalted egg white powder in the 3D printed mixtures. The homogeneous sample consisted of mixture SDE96-Med and the inhomogeneous samples of SDE102 and SDE94-Hi (Table 1). The overall NaCl content of the homogeneous sample (1.20 ± 0.13 g/100 g dry material) was not significantly different ($p > 0.05$) from that of the inhomogeneous samples ($1.30 \pm$
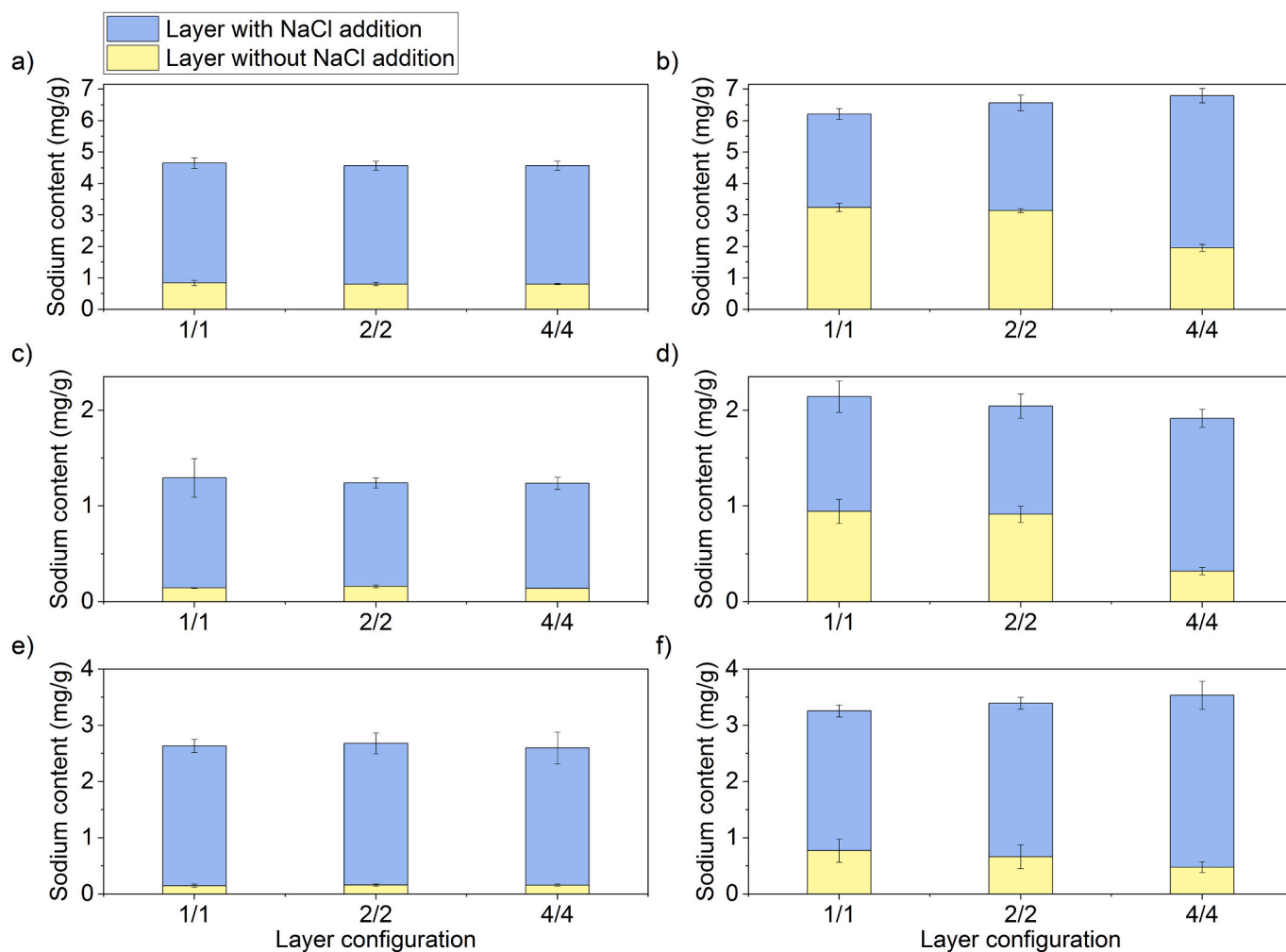

Fig. 7. Sodium content in different sample layers before and after the 3D printing and heating process and storage: (a) starch-based blends consisting of SE60 and SE60-Hi-DYE; (b) 3D printed sample consisting of SE60 and SE60-Hi-DYE; (c) starch-based blends consisting of SDE102 and SDE96-Med-DYE; (d) 3D printed sample consisting of SDE102 and SDE96-Med-DYE; (e) starch-based blends consisting of SDE102 and SDE94-Hi-DYE; and (f) 3D printed sample consisting of SDE102 and SDE94-Hi-DYE.

0.10 g/100 g dry material). Besides, the lowest perceivable difference of the sensory panel was 0.2 g/100 g NaCl on dry material as shown in Section 3.4. During the sensory evaluation, the inhomogeneous samples of all three configurations were perceived significantly saltier than the homogeneous reference sample ($p = 0.026$). This demonstrates that, at an overall NaCl content of ~1.3 g/100 g dry material, a sodium concentration ratio of ~1:6 in case of configuration 4/4, of ~1:4 in case of configuration 2/2, and of ~1:3 in case of configuration 1/1 (Section 3.3) is sufficiently strong to enhance the saltiness perception in layered 3D printed samples. The saltiness enhancement could be attributed to a small extent to an accelerated sodium release from the food matrix, but to a higher extent to the sensory contrast, because alternating stimuli of low and high sodium concentration prevent taste adaption and thus, are more intensively perceived than a continuous stimulus (Konitzer et al., 2013; Noort et al., 2010; Noort, Bult, & Stieger, 2012).

The effect of saltiness enhancement due to spatial NaCl heterogeneity in the 3D printed samples could be applied for sodium reduction in real life products while maintaining the perceived saltiness intensity. Sodium diffusion from the high to the low NaCl layers reduces the initial NaCl concentration ratios. Therefore, high NaCl concentration gradients must be applied while, at the same time, the overall NaCl content must stay at a low level to ensure an enhancement of saltiness perception by inhomogeneous spatial NaCl distribution. To reduce the effect of diffusion in future applications, configuration pattern other than layer

configurations could be used where the ratio of the printing blends with and without salt addition is not balanced but concentrated spots are site-specifically introduced in matrix without salt addition.

4. Conclusion

A 3D printing method was developed that combines texturing, localization, and focused on-board near infrared stabilization of food systems. This 3D SLTS technique enables the production of hydrated starch-egg white powder-material systems in reproducible textural configurations. For the first time, defined NaCl concentration gradients were site-specifically incorporated and locally resolved in 3D printed starch-based food textures. The inhomogeneous spatial sodium chloride distribution caused saltiness enhancement, provided that the sensory contrast was sufficiently strong and the overall NaCl content at a low level. The evolved 3D printing method has the potential to be utilized in the development of healthier products due to sodium reduction without compromising saltiness intensity. Furthermore, the combination of texturing and targeted localization of spatial concentrations gradients could be applied to elucidate not only texture-taste interactions but also texture-aroma interactions. This can be a step forward to customize 3D printed food by systematically influencing texture, taste, and aroma to achieve ideal sensory profiles.

Declaration of Competing Interest

The authors declare that they have no known competing financial interests or personal relationships that could have appeared to influence the work reported in this paper.

Acknowledgements

References

ASTM-International. (2012). Standard terminology for additive manufacturing technologies. In *ASTM F2792-10e1 Standard, Vol ASTM F2792-10e1 Standard*. ASTM International. http://www.ciri.org.nz/nzrma/technologies.html.

Attenburrow, G. E., Goodband, R. M., Taylor, L. J., & Lillford, P. J. (1989). Structure, mechanics and texture of a food sponge. *Journal of Cereal Science, 9*(1), 61–70. https://doi.org/10.1016/S0733-5210(89)80024-4

Baiano, A. (2020). 3D printed foods: A comprehensive review on technologies, nutritional value, safety, consumer attitude, regulatory framework, and economic and sustainability issues. *Food Reviews International, 00*(00). https://doi.org/10.1080/87559129.2020.1762091. Taylor & Francis.

Beer, F. P., Jr., DeWolf, E. R. J., & Mazurek, D. F. (2011). *Statics and mechanics of materials* (1st ed.). McGraw-Hill.

Derossi, A., Caporizzi, R., Azzollini, D., & Severini, C. (2018). Application of 3D printing for customized food. A case on the development of a fruit-based snack for children. *Journal of Food Engineering, 220*, 65–75. https://doi.org/10.1016/j.jfoodeng.2017.05.015

Fahmy, A., Becker, T., & Jekle, M. (2018). 3D printing of cereal-based materials: On the relation between rheology and printability. In *, 18. AACCI Annual Meeting Cereals & Grains*.

Fahmy, A. R., Becker, T., & Jekle, M. (2019). Flow behavior analysis for 3D printing of starch- based systems : Morphological imaging and multiple stage extrusion characterization through a rheometry imitation approach. In *33rd EFFoST International Conference*.

Fahmy, A. R., Becker, T., & Jekle, M. (2020). 3D printing and additive manufacturing of cereal-based materials: Quality analysis of starch-based systems using a camera-based morphological approach. *Innovative Food Science & Emerging Technologies, 63* (April), 102384. https://doi.org/10.1016/j.ifset.2020.102384

Fahmy, A. R., Becker, T., & Jekle, M. (2021). *Design and modulation of food textures using 3D printing of closed-cell foams in point lattice systems*. DECHEMA - Jahrestreffen Lebensmittelverfahrenstechnik.

Fennema, O. R. (1993). *Food chemistry (2nd editio)*. Marcel Dekker Inc.

Ferreira Machado, F., Coimbra, J. S. R., Garcia Rojas, E. E., Minim, L. A., Oliveira, F. C., & Sousa, R. (2007). Solubility and density of egg white proteins: Effect of pH and saline concentration. *LWT - Food Science and Technology, 40*(7), 1304–1307. https://doi.org/10.1016/j.lwt.2006.08.020

Gibson, L. J. (1989). Modelling the mechanical behavior of cellular materials. *Materials Science and Engineering A, 110*(C), 1–36. https://doi.org/10.1016/0921-5093(89)90154-8

Gibson, L. J., & Ashby, M. F. (1999). *Cellular-Solids-Structure-and-Properties-Cambridge-Solid-State-Science-Series-.pdf* (p. 510). https://books.google.pt/books/about/Cellular_Solids.html?id=IySUr5sn4N8C&source=kp_cover&redir_esc=y.

Goesaert, H., Brijs, K., Veraverbeke, W. S., Courtin, C. M., Gebruers, K., & Delcour, J. A. (2005). Wheat flour constituents: How they impact bread quality, and how to impact their functionality. *Trends in Food Science and Technology, 16*(1–3), 12–30. https://doi.org/10.1016/j.tifs.2004.02.011

He, C., Zhang, M., & Fang, Z. (2020). 3D printing of food: Pretreatment and post-treatment of materials. *Critical Reviews in Food Science and Nutrition, 60*(14), 2379–2392. https://doi.org/10.1080/10408398.2019.1641065

ISO 5495. (2005). *Sensory Analysis – Methodology – Paired Comparison Test. Geneva, Switzerland*: International Organization for Standardization. https://www.iso.org/standard/31621.html.

Jekle, M., Mühlberger, K., & Becker, T. (2016). Starch-gluten interactions during gelatinization and its functionality in dough like model systems. *Food Hydrocolloids, 54*, 196–201. https://doi.org/10.1016/j.foodhyd.2015.10.005

Jekle, M., Necula, A., Jekle, M., & Becker, T. (2019). Concentration dependent rate constants of sodium substitute functionalities during wheat dough development. *Food Research International, 116*(August), 346–353. https://doi.org/10.1016/j.foodres.2018.08.047

Jonkers, N., Van Dommelen, J. A. W., & Geers, M. G. D. (2020). Experimental characterization and modeling of the mechanical behavior of brittle 3D printed food. *Journal of Food Engineering, 278*, 109941. https://doi.org/10.1016/j.jfoodeng.2020.109941

Kakalis, L. T., & Regenstein, J. M. (1986). Effect of pH and salts on the solubility of egg white protein. *Journal of Food Science, 51*(6), 1445–1447. https://doi.org/10.1111/j.1365-2621.1986.tb13830.x

Kinsella, J. E. (1982). Structure and functional properties of food proteins. In J. J. C. P. P. Fox (Ed.), *Food proteins (pp. 72–85)*. Applied Science Published.

Konitzer, K., Tabea, P., Oliveira, P., Arendt, E., Koehler, P., & Hofmann, T. (2013). Kinetics of sodium release from wheat bread crumb as affected by sodium distribution. *Journal of Agricultural and Food Chemistry, 61*, 10659–10669. https://doi.org/10.1021/jf404458v

Kramer, A., & Szczesniak, A. S. (Eds.). (1973). *Texture measurement of foods* (1st ed.). Netherlands: Springer. https://doi.org/10.1007/978-94-010-2562-1.

Le Tohic, C., O'Sullivan, J. J., Drapala, K. P., Chartrin, V., Chan, T., Morrison, A. P., … Kelly, A. L. (2018). Effect of 3D printing on the structure and textural properties of processed cheese. *Journal of Food Engineering, 220*, 56–64. https://doi.org/10.1016/j.jfoodeng.2017.02.003

Lille, M., Nurmela, A., Nordlund, E., Metsä-Kortelainen, S., & Sozer, N. (2018). Applicability of protein and fiber-rich food materials in extrusion-based 3D printing. *Journal of Food Engineering, 220*, 20–27. https://doi.org/10.1016/j.jfoodeng.2017.04.034

Liu, Y., Yu, Y., Liu, C., Regenstein, J. M., Liu, X., & Zhou, P. (2019). Rheological and mechanical behavior of milk protein composite gel for extrusion-based 3D food printing. *Lwt, 102*, 338–346. https://doi.org/10.1016/j.lwt.2018.12.053

Liu, Z., Zhang, M., & Yang, C. (2018). Dual extrusion 3D printing of mashed potatoes/strawberry juice gel. *Lwt, 96*, 589–596. https://doi.org/10.1016/j.lwt.2018.06.014

Liu, Z., Chen, H., Zheng, B., Xie, F., & Chen, L. (2020). Understanding the structure and rheological properties of potato starch induced by hot-extrusion 3D printing. *Food Hydrocolloids*, 105812. https://doi.org/10.1016/j.foodhyd.2020.105812

Mmadi, M., Amza, T., Wang, Y. C., & Zhang, M. (2014). Effect of desalination on physicochemical and functional properties of duck (Anas plotyrhyncus) egg whites. *Advance Journal of Food Science and Technology, 6*(6), 784–791. https://doi.org/10.19026/ajfst.6.111

Noort, M. W. J., Bult, J. H. F., & Stieger, M. (2012). Saltiness enhancement by taste contrast in bread prepared with encapsulated salt. *Journal of Cereal Science, 55*(2), 218–225. https://doi.org/10.1016/j.jcs.2011.11.012

Noort, M. W. J., Bult, J. H. F., Stieger, M., & Hamer, R. J. (2010). Saltiness enhancement in bread by inhomogeneous spatial distribution of sodium chloride. *Journal of Cereal Science, 52*(3), 378–386. https://doi.org/10.1016/j.jcs.2010.06.018

Paulik, S., Yu, W. W., Flanagan, B., Gilbert, R. G., Jekle, M., & Becker, T. (2019). Characterizing the impact of starch and gluten-induced alterations on gelatinization behavior of physically modified model dough. *Food Chemistry, 301*, 125276. https://doi.org/10.1016/j.foodchem.2019.125276

Peleg, M. (2019). The instrumental texture profile analysis revisited. *Journal of Texture Studies, 50*(5), 362–368. https://doi.org/10.1111/jtxs.12392

Phuhongsung, P., Zhang, M., & Devahastin, S. (2020). Influence of surface pH on color, texture and flavor of 3D printed composite mixture of soy protein isolate, pumpkin, and beetroot. *Food and Bioprocess Technology, 13*(9), 1600–1610. https://doi.org/10.1007/s11947-020-02497-8

Pulatsu, E. T., Su, J., Lin, J., & Lin, M. (2020). Factors affecting 3D printing and post-processing capacity of cookie dough. *Innovative Food Science and Emerging Technologies, 102316*. https://doi.org/10.1016/j.ifset.2020.102316

Riadh, M. H., Ahmad, S. A. B., Marhaban, M. H., & Soh, A. C. (2015). Infrared heating in food drying: An overview. *Drying Technology, 33*(3), 322–335. https://doi.org/10.1080/07373937.2014.951124

Skjöldebrand, C., Ellbjär, C., Andersson, C. G., & Eriksson, T. S. (1988). Optical properties of bread in the near-infrared range. *Journal of Food Engineering, 8*(2), 129–139. https://doi.org/10.1016/0260-8774(88)90059-3

Sun, J., Zhou, W., Yan, L., Huang, D., & Lin, L. ya.. (2018). Extrusion-based food printing for digitalized food design and nutrition control. *Journal of Food Engineering, 220*, 1–11. https://doi.org/10.1016/j.jfoodeng.2017.02.028

Thammasena, R., Fu, C. W., Liu, J. H., & Liu, D. C. (2020). Evaluation of nutrient content, physicochemical and functional properties of desalted duck egg white by ultrafiltration as desalination. *Animal Science Journal, 91*(1), 1–9. https://doi.org/10.1111/asj.13339

Tournier, C., Sulmont-rossé, C., & Guichard, E. (2007). Flavour perception: Aroma, taste and texture interactions. *Food, 1*, 246–257.

Vancauwenberghe, V., Delele, M., Vanbiertvliet, J., Aregawi, W., Verboven, P., & Lammertyn, J. (2018). Model-based design and validation of food texture of 3d printed pectin-based food simulants. *Journal of Food Engineering, 231*, 72–82. https://doi.org/10.1016/j.jfoodeng.2018.03.010

Vancauwenberghe, V., Mbong, V. B. M., Vanstreels, E., Verboven, P., Lammertyn, J., & Nicolai, B. (2019). 3D printing of plant tissue for innovative food manufacturing: Encapsulation of alive plant cells into pectin based bio-ink. *Journal of Food Engineering, 263*, 454–464. https://doi.org/10.1016/j.jfoodeng.2017.12.003

Wang, K. (2012). Die swell of complex polymeric systems. In J. De Vicente (Ed.), *Viscoelasticity - From Theory to Biological Applications (1st ed., issue 1, pp. 77–96)*. IntechOpen. https://doi.org/10.5772/50137.

Wegrzyn, T. F., Golding, M., & Archer, R. H. (2012). Food layered manufacture: A new process for constructing solid foods. *Trends in Food Science and Technology, 27*(2), 66–72. https://doi.org/10.1016/j.tifs.2012.04.006

Yang, F., Zhang, M., & Liu, Y. (2019). Effect of post-treatment microwave vacuum drying on the quality of 3D-printed mango juice gel. *Drying Technology, 37*(0), 1757–1765. https://doi.org/10.1080/07373937.2018.1536884

Yang, F., Zhang, M., Prakash, S., & Liu, Y. (2018). Physical properties of 3D printed baking dough as affected by different compositions. *Innovative Food Science & Emerging Technologies, 49*, 202–210. https://doi.org/10.1016/J.IFSET.2018.01.001

Zghal, M. C., Scanlon, M. G., & Sapirstein, H. D. (2002). Cellular structure of bread crumb and its influence on mechanical properties. *Journal of Cereal Science, 36*(2), 167–176. https://doi.org/10.1006/jcrs.2001.0445

Zhang, L., Lou, Y., & Schutyser, M. A. I. (2018). 3D printing of cereal-based food structures containing probiotics. *Food Structure, 18*(August), 14–22. https://doi.org/10.1016/j.foostr.2018.10.002